Journal of Nuclear Materials 478 (2016) 176–184

Contents lists available at ScienceDirect

Journal of Nuclear Materials

journal homepage: www.elsevier.com/locate/jnucmat

Correlation between crystallographic orientation and surface faceting in UO_2

Yinbin Miao [a], Kun Mo [a, *], Tiankai Yao [b], Jie Lian [b, **], Jeffrey Fortner [a], Laura Jamison [a], Ruqing Xu [a], Abdellatif M. Yacout [a]

[a] Argonne National Laboratory, Lemont, IL 60439, United States
[b] Rensselaer Polytechnic Institute, Troy, NY 12180, United States

HIGHLIGHTS

- Crystallographic orientation -surface faceting correlation is established for UO_2.
- Equilibrium UO_2 surface is dominated by triple-plane structures.
- Surface morphology may also be influenced by local fluctuation of hydroxidation.
- A method to measure crystallographic orientation using SE images is proposed.

GRAPHICAL ABSTRACT

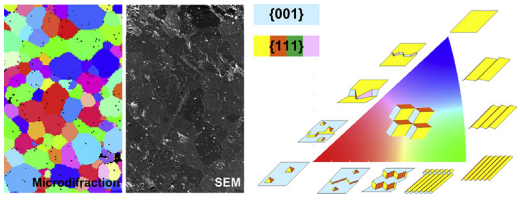

ARTICLE INFO

Article history:
Received 5 April 2016
Received in revised form
27 May 2016
Accepted 31 May 2016
Available online 6 June 2016

Keywords:
Uranium dioxide
Surface faceting
Morphology
Synchrotron diffraction
Scanning electron microscopy

ABSTRACT

Here coordinated experimental efforts to quantitatively correlate crystallographic orientation and surface faceting features in UO_2 are reported upon. A sintered polycrystalline UO_2 sample was thermally etched to induce the formation of surface faceting features. Synchrotron Laue microdiffraction was used to obtain a precise crystallographic orientation map for the UO_2 surface grains. Scanning electron microscopy (SEM) was utilized to collect the detailed information on the surface morphology of the sample. The surface faceting features were found to be highly dependent on the crystallographic orientation. In most cases, Triple-plane structures containing one {100} plane and two {111} planes were found to dominate the surface of UO_2. The orientation-faceting relationship established in this study revealed a practical and efficient method of determining crystallographic orientation based on the surface features captured by SEM images.

1. Introduction

Surface properties of UO_2 play an important role throughout the lifetime of this widely-used commercial nuclear fuel material, from manufacturing to storage. The surface features and corresponding thermodynamic characteristics influence the morphology, size, and distribution of fission gas bubbles as well as the initiation and propagation of micro-fractures within the nuclear fuel pellets. Hence, a better understanding of the surface behavior of UO_2 will help interpret the in-pile behavior of UO_2, thereby advancing the capability of precisely predicting fuel performance [1–3]. Like many other materials, the surface energy of UO_2 varies substantially with crystallographic orientation. This energy variation creates anisotropy in surface energy, which leads to the formation of surface faceting features during annealing. Detailed understanding

* Corresponding author.
** Corresponding author.
E-mail addresses: kunmo@anl.gov (K. Mo), lianj@rpi.edu (J. Lian).

http://dx.doi.org/10.1016/j.jnucmat.2016.05.044
0022-3115/

of these orientation-dependent surface faceting features can not only expand the fundamental knowledge of the surface characteristics of UO_2, but can also shine a light on the mechanisms involved in gas swelling and micro-fracture of UO_2 fuel [4,5]. Additionally, by establishing a deterministic correlation between the crystallographic orientation and surface morphology, it is possible to develop a method to deduce the lattice orientation of surface grains of a UO_2 sample based on its surface faceting features.

As a consequence of anisotropic surface energy, the surface faceting phenomenon occurs in a great number of crystalline materials. The surface faceting features can also be correlated with the Wulff shape of the crystal [6]. The formation mechanism for surface faceting has been investigated by both experimental and computational approaches [7–10]. Previously, the surface faceting of UO_2 was investigated by low energy electron diffraction (LEED). However, as LEED is limited to the characterization of single crystal specimens, only those planes with low Miller indices; namely, {100}, {110}, and {111} planes; have been examined [11–14]. As the closest packed layer, the {111} surface of UO_2 has the lowest surface energy [15,16] and is, therefore, not subject to surface coarsening or faceting [17]. On the contrary, the {110} surface forms a wavy structure consisting of two {111} planes sharing a <110> edge with the angle of 109.47° as a result of annealing. In addition, although the majority of the {100} surface remains smooth during annealing, hemi-octahedra (square pyramids) that contain four {111} planes, form on the {100} surface. These pyramid features are believed to be due to the deposition of UO_2 vapor, which is generated during annealing. Only {111} and {100} planes are present at equilibrium, while the {110} and higher-index planes are absent. All the edges present on equilibrium UO_2 surfaces are <110> type, as reported by previous studies [14]. The dominance of the {111} and {100} planes and the <110> edge is also comparable to previous studies of the morphology of UO_2 single crystal. Theoretical prediction gives a simple {111} faceted octahedron [15]. Meanwhile, the experimental examination is limited to some SEM observation of voids on UO_2 surfaces, which shows a {111} faceted octahedron truncated by {100} planes [18,19]. The appearance of {100} planes might be explained by non-equilibrium kinetics model [15] or the modification of surface energy due to hydroxidation [20,21]. Hence, further studies are necessary to clarify the morphology of UO_2 crystal. Recently, the {100} and {111} surfaces were characterized by scanning tunneling microscopy (STM), revealing the atomic level structure of these low-index crystallographic planes [22,23].

All previous investigations on the surface faceting features of UO_2 are limited to three low Miller index planes present within single crystal specimens. There is a scarcity of comprehensive studies on the faceting features of surfaces with general indices. In order to develop a comprehensive understanding of the faceting behavior of polycrystalline UO_2, two key properties need to be determined: the crystallographic orientation of the grains, and a quantitative description of their corresponding surface faceting features. The coarse surface of UO_2 with faceting features limits the utilization of conventional techniques. For instance, although electron backscattering diffraction (EBSD) is capable of working with coarse surfaces, the faceting features may create shadows on investigated surfaces, preventing the collection of grain to grain matching maps of crystallographic orientation, especially when grains are small. However, synchrotron X-ray diffraction is barely influenced by surface roughness due to the deep penetration ability originating from its high energy and intensity, making it an ideal technique for this study. This synchrotron technique has been adopted to examine a variety of bulk materials, including advanced Fe-based alloys [24–29] and metallic nuclear fuel materials [30,31]. When the X-ray beam is focused to a submicron size, mapping of a micrograined specimen can be easily achieved [32]. Thus, synchrotron Laue microdiffraction [33] has the unique non-destructive capability of measuring the crystallographic orientation of grains with coarse surfaces. The surface features can be characterized by secondary electron (SE) imaging with a scanning electron microscope (SEM). Synchrotron microdiffraction and SE SEM techniques were coordinated in this study to establish the precise correlation between crystallographic orientation and the surface faceting features of multiple grains within a polycrystalline UO_2 specimen.

2. Experiments

2.1. Specimen preparation

The polycrystalline UO_2 specimen investigated in this study was fabricated utilizing spark plasma sintering (SPS) [34]. UO_2 powder was procured from International Bio-analytical Industries Inc. To reduce the particle size, the powders were ball milled for 30 min utilizing tungsten carbide container and milling balls. To produce bulk UO_2 samples, an SPS within an industrial argon atmosphere (<5 ppm oxygen) was used. The temperature was increased to 1600 °C with a 100 °C/min ramp rate, while the pressure was increased from a 10 MPa pre-load to 40 MPa. The sample was sintered for 5 min under these conditions, and then the temperature was decreased to 1500 °C at 20 °C/min as the pressure was decreased to 10 MPa. The sample was annealed for 30 min under these conditions in order to relieve residual stresses induced during sintering. The power was turned off, and the sample was allowed to cool to room temperature. Further details about the ball milling and SPS procedures can be found in Ref. [34]. The sintered UO_2 sample was mechanically polished down to 0.5 μm roughness using diamond lapping films to produce a uniformly smooth surface finish. The sample was then thermally etched by annealing at 1500 °C for 1 h in a He gas environment to activate the formation of surface faceting by enhancing surface diffusion. By measuring the lattice parameter using an PANalytical X-ray diffractometer, the stoichiometry of the sample was determined according to the following equation: $a = 5.4705 - 0.132x$ [35,36], where a is the derived lattice parameter, and x is the stoichiometry parameter as in the formula UO_{2+x}. The stoichiometry of the sample investigated in this study was found to be $UO_{2.00047\pm0.00608}$. No distinguishable oxygen pickup was detected during the thermal etching procedure based on the lattice parameter measurement.

2.2. Synchrotron microdiffraction

Synchrotron Laue microdiffraction measurements were performed at Sector 34-ID-E at the Advanced Photon Source (APS), Argonne National Laboratory (ANL). The synchrotron experiment setup is illustrated in Fig. 1(a). The UO_2 specimen was kept in a sealed container with a Kapton film window. The synchrotron white X-ray beam was focused by a Kirkpatrick-Baez (K-B) mirror system to provide a 0.6 μm × 0.8 μm beam size for 2D scanning. The sample was oriented such that the sample surface was at a 45° angle to the beam direction. Laue diffraction patterns were collected by a 2048 × 2048 2D area detector at an array of points across the sample. The Laue patterns were then processed to determine the reciprocal lattice vectors so that the crystal orientation of all the scanned positions could be derived. The scanning step length in both directions was 2 μm. Because the grain size of the UO_2 sample was 18.93 ± 1.28 μm according to the SEM images, approximately 70 data points were collected for each grain.

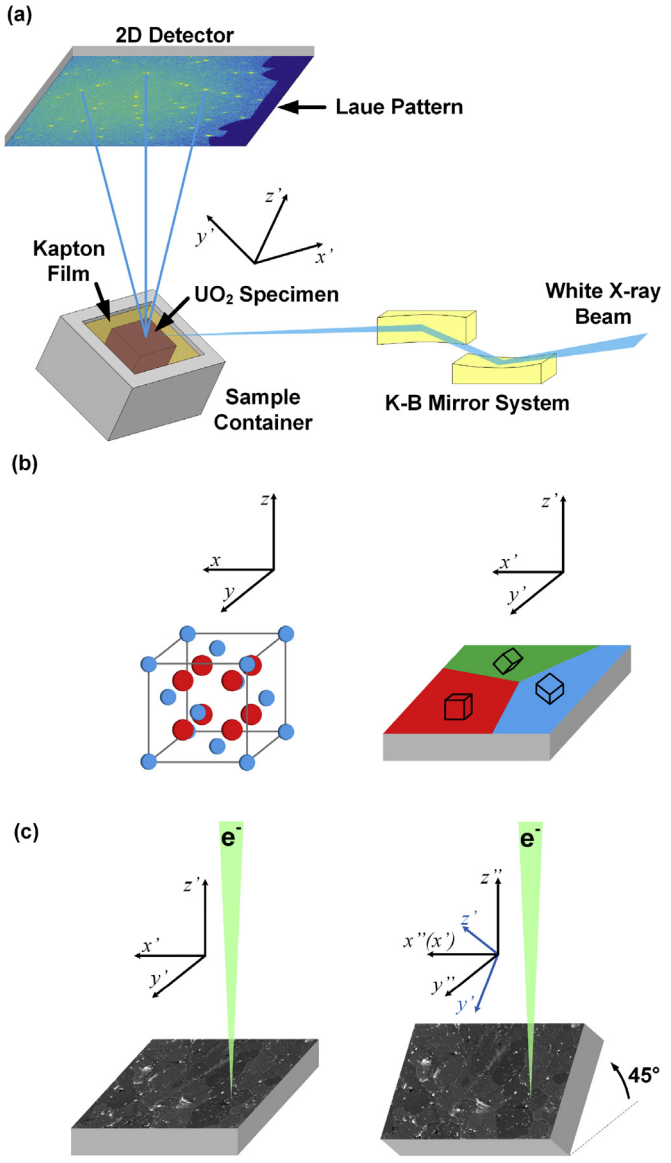

Fig. 1. the experiment setups: (a) the setup of the synchrotron Laue microdiffraction experiment; (b) the relationship between the lattice coordinate system of UO_2 with fluorite structure (left) and the specimen coordinate system (right): each grain in the specimen has its own lattice coordination system and corresponding Euler angles for transformation to the specimen coordinate system; (c) the tilting setup of the SEM investigations: the specimen coordinate system (′) and tilted specimen coordinate system (″) are shown in this figure: the z' direction is the surface normal.

2.3. Surface analysis

The surface morphology of the UO_2 specimen was captured by a Hitachi S-3000N SEM. As the SEM only captures 2D projections of 3D surface features, the specimen was tilted to two angles (0° and 45°) for the regions of interest, to avert the loss of information during projection, as shown in Fig. 1(c). The tilting axis is the x-axis of the specimen coordination system (x').

Previous investigations on both surface faceting and morphology of UO_2 at equilibrium showed the dominance of {111} planes as well as the coexistence of {100} planes. However, {110} surfaces, and surfaces with higher Miller indices were not observed at equilibrium [14]. Therefore, the {111} and {100} planes are assumed to be the dominant surface facets for analysis in this study, namely, all the edges observed are assumed to be <110> type.

Any orientation of a UO_2 lattice can be described by three Euler angles: ϕ, θ and ψ, representing three rotation operations, respectively. Any point in the lattice coordinate system, $P=[x,y,z]^T$, can be transformed into the corresponding coordinates in the specimen coordinate system, $P'=[x',y',z']^T$ through the Euler rotations described by the following expression (x-convention):

$$P' = \begin{pmatrix} cos\psi & sin\psi & 0 \\ -sin\psi & cos\psi & 0 \\ 0 & 0 & 1 \end{pmatrix} \begin{pmatrix} 1 & 0 & 0 \\ 0 & cos\theta & sin\theta \\ 0 & -sin\theta & cos\theta \end{pmatrix} \times \begin{pmatrix} cos\phi & sin\phi & 0 \\ -sin\phi & cos\phi & 0 \\ 0 & 0 & 1 \end{pmatrix} P \quad (1)$$

Because the specimen was also tilted to 45° in SEM, the coordinate of the point in the tilted specimen coordinate system (45°), $P''=[x'',y'',z'']^T$ experiences an extra rotation operation:

$$P'' = \begin{pmatrix} 1 & 0 & 0 \\ 0 & \frac{1}{\sqrt{2}} & -\frac{1}{\sqrt{2}} \\ 0 & \frac{1}{\sqrt{2}} & \frac{1}{\sqrt{2}} \end{pmatrix} P' \quad (2)$$

As mentioned previously, <110> are assumed to be the dominant edges on the UO_2 surfaces, and all six <110> edges were considered in this study. These six <110> edges can be defined by 5 points in the lattice coordinate system: $P_0 = [0,0,0]^T$, $P_1=[-1,0,-1]^T$, $P_2=[1,0,-1]^T$, $P_3=[0,-1,-1]^T$, and $P_4=[0,1,-1]^T$. If $L_{ij}=P_j-P_i=[x_j-x_i,y_j-y_i,z_j-z_i]^T$ represents the direction vector of the edge defined by the two points P_i and P_j, the six unique <110> edges are respectively L_{01}, L_{02}, L_{03}, L_{04}, L_{13}, and L_{14}. In the specimen coordinate system (0°), those L_{ij} become $L'_{ij}=P'_j-P'_i$ from Equation (1). At a 45° tilt in the SEM, the corresponding direction vectors of the <110> edges are $L''_{ij}=P''_j-P''_i$, as described in Equation (2). Because the information of the third component ($z'_j-z'_i$ and $z''_j-z''_i$) of the edge direction vector is lost during the 2D projection in SEM imaging, the first and second components of L'_{ij} and L''_{ij} determine the direction of the specific <110> edges observed in SEM images. Polar coordinates were used to define the <110> edges in the SEM images. The polar angles are defined as: $l'_{ij}=atan2(y'_j-y'_i,x'_j-x'_i)$ (zero tilt) and $l''_{ij}=atan2(y''_j-y''_i,x''_j-x''_i)$ (45° tilt), where $atan2$ is the two-argument arctangent function.

3. Results

3.1. Orientation-dependent surface faceting

An approximately 250 μm × 400 μm region of the polycrystalline UO_2 specimen was selected to perform both Laue microdiffraction and SEM measurements (Fig. 2). The orientation map with inverse pole figure (IPF) coloring from the Laue microdiffraction patterns was compared to the surface topography images obtained by the SEM. Grain to grain matching between the two images confirmed that both techniques captured the same region on the specimen. Based on the orientation information obtained by microdiffraction, the surface faceting features can be correlated to the crystallographic orientation of each individual grain.

The presence of surfaces with low Miller indices ({100}, {110} and {111}) that were observed in previous studies was confirmed. Due to the unique nature of this study, a much broader range of surface normal orientations were able to be observed. The unique surface features of these orientations were mapped out on the standard stereographic triangle (SST), and are described in the following paragraph. Fig. 3 elucidates the change in surface

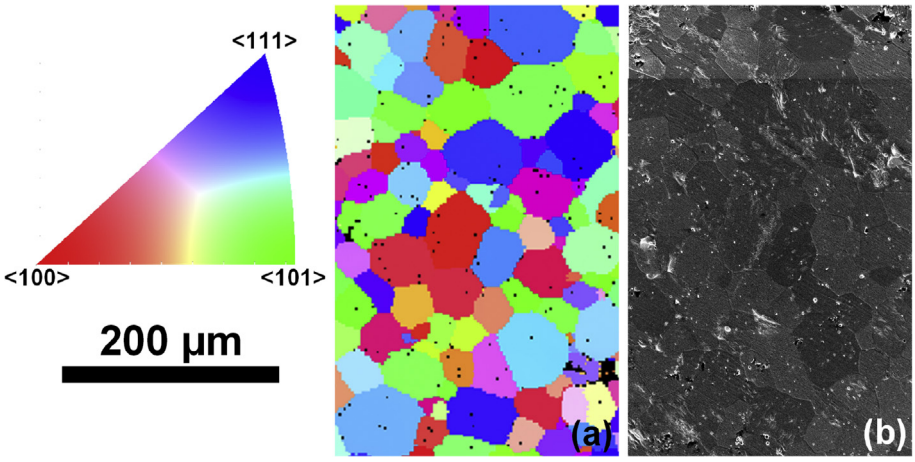

Fig. 2. Same region in the UO_2 specimen characterized by synchrotron Laue microdiffraction and SEM: (a) orientation map determined by Laue microdiffraction patterns with inverse pole figure (IPF) coloring. The black spots represent those positions of which crystallographic orientations failed to be indexed; (b) SEM secondary electron image.

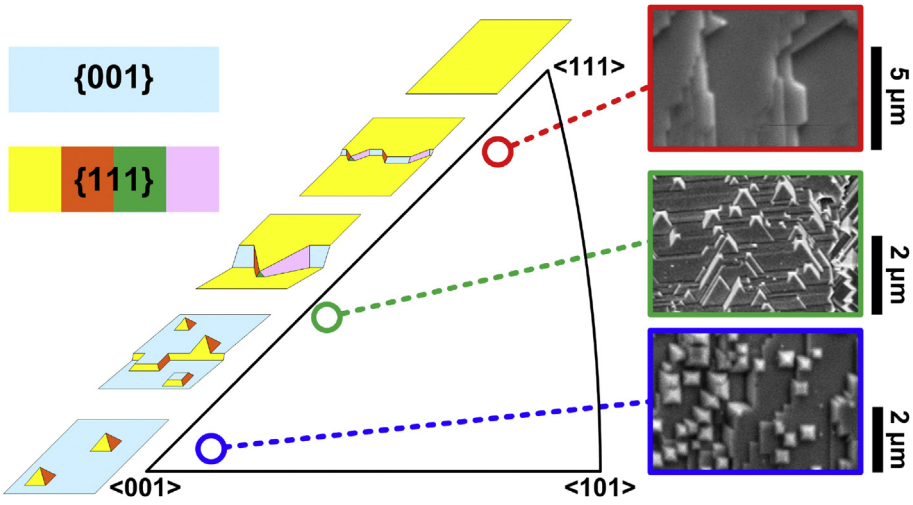

Fig. 3. Surface faceting features with surface normal from <100> tilting to <111>: surface morphology was illustrated by both schematics and SEM images on the SST.

morphology as the surface normal changes from <001> to <111>, along a <110> axis (on side of the SST). When the surface normal is near <001>, the surface is dominated by a {100} plane with a series of hemi-octahedra made of four {111} planes (see the blue point in Fig. 3). The large pyramids sometimes are truncated by a {100} plane to form a frustum. When the surface normal is slightly inclined from <001>, the pyramids are also inclined, and the surface becomes stepped by {111} planes (see the green point in Fig. 3). As the surface normal becomes closer to <111>, the fraction of {111} planes increases. When the surface normal is close to <111>, the surface is dominated by a {111} plane, with steps formed by a {100} plane, and residual inclined pyramids or frusta(see the red point in Fig. 3). When the surface normal is perfectly <111>, it is theoretically a smooth {111} plane.

Fig. 4 shows the evolution of the surface morphology as the surface normal evolves from <001> to <101> along a <010> axis. When the surface normal is near <001>, the dominant feature is still a stepped {100} plane with {111} square pyramids or frusta. However, as the surface normal tilts towards <101>, the steps are no longer dominated by one {111} plane (as occurred when the surface normal was tilted towards <111>), but split between two {111} planes (see the red point in Fig. 4). As the surface normal

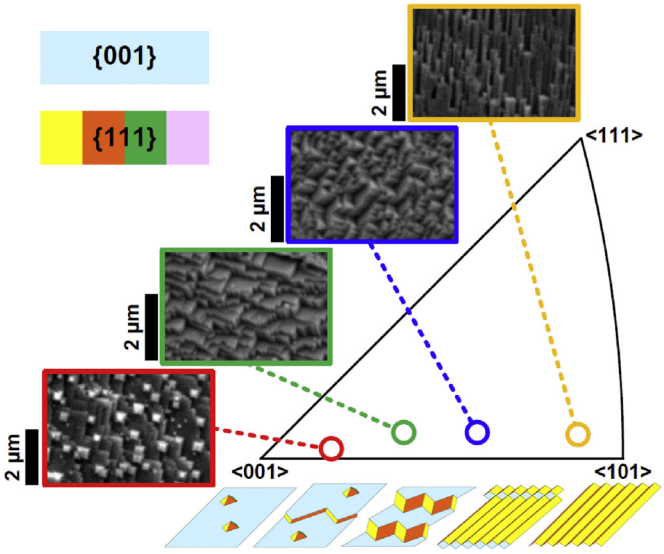

Fig. 4. Surface faceting features with surface normal from <100> tilting to <110>: surface morphology was illustrated by both schematics and SEM images on the SST.

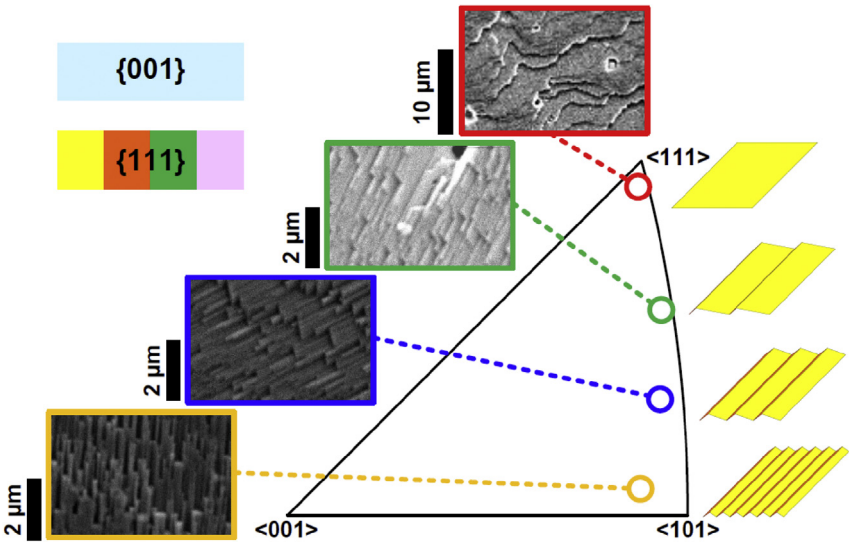

Fig. 5. Surface faceting features with surface normal from <111> tilting to <110>: surface morphology was illustrated by both schematics and SEM images on the SST.

approaches <101>, the proportion of the two {111} planes continues to increase, as illustrated by the green and blue points in Fig. 4. When the surface normal is close to <101>, the surface is dominated by a wavy feature containing two {111} planes and stepped by a {100} plane (see the orange point in Fig. 4).

Fig. 5 tracks the surface morphology as the surface normal changes from <111> to <101> along a $<10\bar{1}>$ axis. As the surface normal tilts from <111> to <101>, the original {111} plane starts to be stepped by another {111} plane with a 107.49° angle. When the surface normal is close to <101>, the fractions of the two types of {111} planes are equal, creating the characteristic wavy features of the {110} surface. It is worth mentioning that the {100} planes are present in the SEM images in Fig. 5 because the surface normal is not exactly on the side.

After investigating the surface faceting features near the three vertexes and along the three boundaries of the SST, regions with a surface normal falling in the core area of the SST were also examined. Multiple surface normal vectors within this area were studied, some representative cases of which are shown in Fig. 6. For all those cases, two {111} planes and one {100} plane are present with three <110> edges, forming the so-called triple-plane structure, as defined in this study. The fraction of each plane type is determined by the specific position on the SST. For example, if the surface normal is relatively close to <001>, the {100} plane is dominant (see the red point in Fig. 6). Similarly, if the surface normal is relatively close to <111>, a {111} plane is dominant (see the green point in Fig. 6), and if the surface normal is relatively close to <101>, two {111} planes are equally dominant to form a wavy feature, as shown by the blue point in Fig. 6.

Therefore, the triple-plane structure is the main component of UO_2 surfaces with general surface normals. Even the smooth {111}/{100} surface and the wavy {110} surface can be regarded as

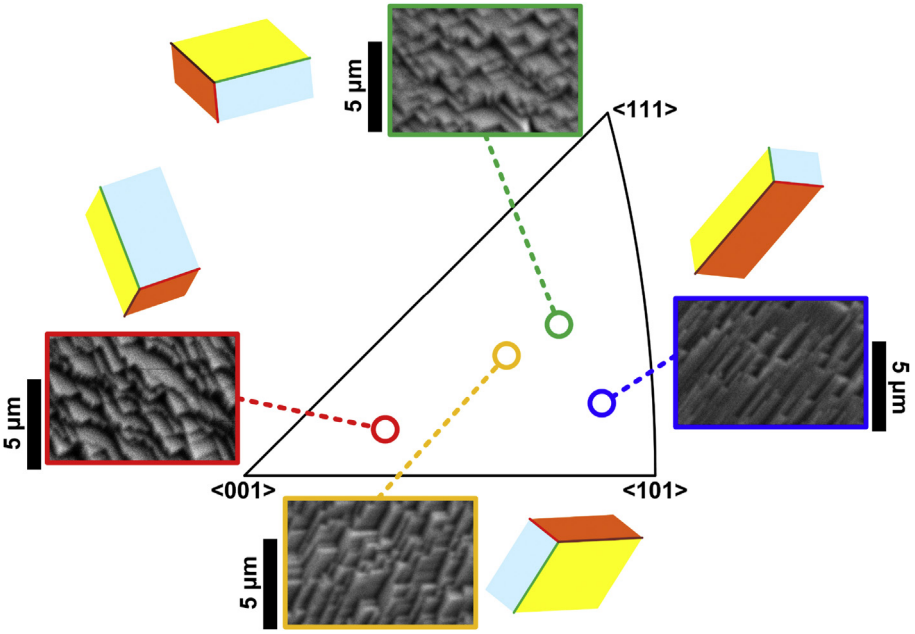

Fig. 6. Surface faceting features with surface normal far away from the edges: surface morphology was illustrated by both schematics and SEM images on the SST.

variants of the triple-plane structure, where one or two of the three planes is overwhelmingly dominant. The only exception occurs when the surface normal is close to <100>, where the {100} plane can be elaborated by square pyramids or frusta. According to previous calculations of surface energies of the {111}, {100}, and {110} planes of UO_2 [15,16], the {111} plane has the lowest surface energy, whereas the {100} plane has the highest surface energy among the three planes of lowest Miller indices. As the closest packed layer of the fluorite structure, the {111} plane has lower surface energy compared to the {110} plane. The wavy feature consisting of two {111} planes, which have an angle of 109.47°, is preferentially formed over a smooth {110} plane once $\gamma_{110} > \sqrt{3/2}\gamma_{111}$. The inequality is satisfied according to the surface energy calculations [15,16], explaining the absence of {110} planes throughout the studies on UO_2 surfaces, including the present one. Due to a relatively higher surface energy, {100} planes can be replaced by a square pyramid composed of four {111} planes as long as $\gamma_{100} > \sqrt{3}\gamma_{111}$. This can be confirmed by the fact that {100} planes are usually accompanied by a series of pyramids. However, a great fraction of {100} planes are still smooth and free of square pyramids or frusta, showing that $\gamma_{100} < \sqrt{3}\gamma_{111}$. This controversy in surface energy anisotropy also determines whether the Wulff shape of UO_2 is truncated by {100} planes or not. According to both DFT and empirical calculation of surface energy anisotropy of UO_2 [15,16], γ_{100} is much larger than $\sqrt{3}\gamma_{111}$. A recent STM investigation on the {100} surface of UO_2 showed that the "smooth" {100} surface is actually covered by trenches of atomic level {111} facets [23]. Accordingly, the effective surface energy of {100} plane, γ_{100}^{eff} is reduced but still exceeds $\sqrt{3}\gamma_{111}$[21]. However, the surface of UO_2 can be hydroxidized. Computational results show that γ_{100}^{eff} can be lower than $\sqrt{3}\gamma_{111}$ once their surfaces are partially or entirely hydroxidized [20,21]. Therefore, the coexistence of faceting and smooth features on {100} surface actually originates from the local fluctuation of surface hydroxidation. On the other hand, the triple-plane structure does always include one {100} plane, rather than three {111} planes, regardless to the local hydroxidation situation. This is because that the three {111} plane structure inevitably involves an acute angle (70.53°) between planes, compromising its space efficiency in covering surfaces. All the surface energy values discussed here are also listed in Table 1.

3.2. Determination of orientation based on SEM images

Based on the assumption of the dominance of the <110> edges on UO_2 surface, the surface morphology has been determined as described above. To validate this assumption, the crystallographic orientations of particular grains were derived directly based on its surface morphology, and then compared with the synchrotron-based experimental data. As all the edges on the surface are <110> edges, the algorithm is based on the measured projected directions of <110> edges ($l_{ij}^{'exp}$ and/or $l_{ij}^{''exp}$). For a specific combination of Euler angles (φ, θ, and ψ), the theoretical direction vectors of the <110> edges ($L_{ij}^{'}$ and $L_{ij}^{''}$) can be calculated according to Equations (1) and (2). The angles of the SEM projections of the <110> edges, $l_{ij}^{'th}$ and $l_{ij}^{''th}$, can be deduced from the first two components of $L_{ij}^{'}$ and $L_{ij}^{''}$. A least squares estimation was used to obtain the optimized combination of Euler angles that minimize the following expression:

$$\sum_{ij}\left(l_{ij}^{'th}-l_{ij}^{'exp}\right)^2+\sum_{ij}\left(l_{ij}^{''th}-l_{ij}^{''exp}\right)^2 \tag{3}$$

The summation was done over all the measurable <110> edges on the SEM images. At minimum, a pair of <110> edges at both 0° and 45° tilting angles are required for the least squares estimation. In this study, a mesh with 1° increment for all three Euler angles was used to approach the optimized combination. The misorientation (δ) between the optimized crystallographic orientation and the microdiffraction measured crystallographic orientation was used to evaluate the accuracy of the fit. The reciprocals of the values of Equation (3) for all possible combinations of Euler angles were used to evaluate the sensitivity of the fitting. In order to visualize the sensitivity examination, the reciprocals were shown in the SST according to the surface normals determined by the Euler angles. Since multiple combinations of Euler angles may share one point on the SST, only the maxima reciprocals were illustrated. The quality of the fit was further evaluated by analyzing the condition number of the Jacobian matrix of the least squares estimation at the optimized point. According to the non-linear least squares estimation theory, the Jacobian matrix has the following components:

$$J_{ij}=\frac{\partial F_i}{\partial x_j}, \tag{4}$$

where, F_i can be any measurable $l_{ij}^{'th}$ or $l_{ij}^{''th}$, and x_j can be ϕ, θ, or ψ. The condition number, c, of the Jacobian matrix J is defined as the ratio between the maximum and minimum singular values of J. The singular values were calculated by singular value decomposition of the Jacobian matrix:

$$J_{m\times n}=U_m\Sigma_{m\times n}V_n^T(m\geq n), \tag{5}$$

$$\Sigma_{m\times n}=\begin{pmatrix}S_n\\0\end{pmatrix},$$

where U_m and V_n are two unitary matrices, $S_n = diag\{\sigma_1,\sigma_2,\ldots,\sigma_n\}$ with $\sigma_1\geq\sigma_2\geq\ldots\geq\sigma_n$ is a diagonal matrix containing the singular values. Determined by the three Euler angles, $n = 3$. Therefore, $c = \sigma_1/\sigma_3$. The number of non-zero singular values indicates the number of fitting parameters (Euler angles) that can be uniquely determined. If σ_3 is non-zero but small, namely, the condition number is large, the Jacobian matrix is ill-conditioned, implying that the optimization results are influenced by the errors in measurement. Otherwise, the Jacobian matrix is well-conditioned, indicating that the optimization is robust.

When the surface normal is close to <100>, due to the existence of the pyramids, all six <110> edges are visible in SEM images. Therefore, no tilting is needed to determine the crystallographic orientation. The fitting result is compared with the synchrotron measured orientation in Fig. 7. The sensitivity of this category of fitting is quite good according to the mapping of the reciprocal least squares. The condition number of the Jacobian matrix is as low as

Table 1
Surface energies of UO_2 surfaces of different indices.

{111}	{100} (flat)	{100} (trench)	{110}	Ref.	Comments
1.18	2.35	n/a	1.74	[15]	Empirical potential
0.27	1.04	n/a	0.73	[16]	DFT
1.29	2.85	2.45	2.04	[21]	Empirical potential
0.85	1.54	1.18	1.21	[21]	Empirical potential; 50% surface hydroxidation

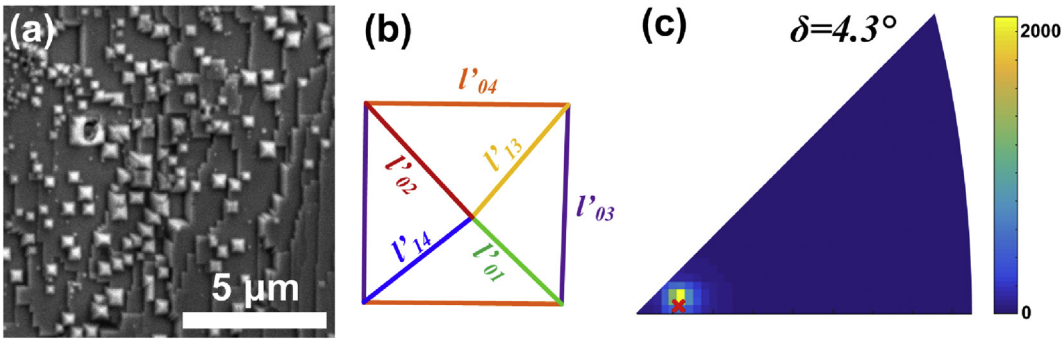

Fig. 7. Fitting details of a typical grain with a surface normal near <100>: (a) the SEM image of a grain with surface normal close to <100>; (b) schematic indicating the six measurable <110> edges in (a); (c) the reciprocals of Equation (3) with surface normal vectors throughout the SST. The red cross marks the crystallographic orientation determined by synchrotron diffraction. (For interpretation of the references to colour in this figure legend, the reader is referred to the web version of this article.)

12.4. The only exception occurs as the surface normal is exactly at <100>, namely, $\theta = 0$ and only $\psi + \phi$ can be uniquely determined, this also results in a zero σ_3, implying that only two of three Euler angles can be uniquely determined.

In most cases, the triple-plane structure dominates the surface morphology. Thus, only three of six <110> edges are visible on the surface. Assuming the three observable edges are L_{01}, L_{02}, and L_{04}, SEM images from both tilting angles (0° and 45°) were used for determining the Euler angles. Because one {100} plane and two {111} planes are involved, the plane types need to be assumed prior to any fitting. There are three possible combinations of plane types that fulfill the triple-plane structure requirements. All three combination are taken into consideration, and the combination that minimizes Equation (3) is regarded as the optimized solution. Fig. 8 illustrates the fitting details of a typical three-plane structure case. All three possible triple-plane structures were fitted, and only one

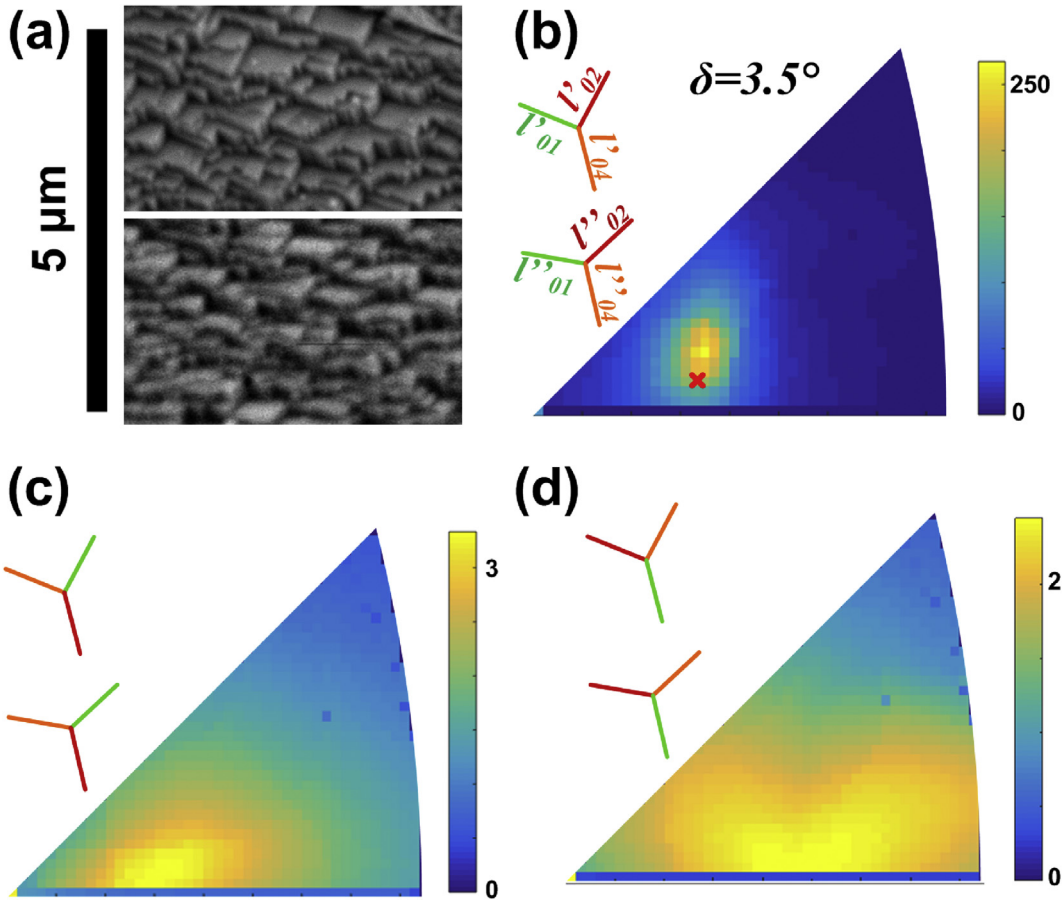

Fig. 8. Fitting details of a typical three-plane feature with three measurable <110> edges: (a) the SEM image of a grain with the triple-plane surface feature; (b) the correct combination of the three measurable <110> edges and the corresponding reciprocals of Equation (3) with surface normal vectors throughout the SST. The red cross marks the crystallographic orientation determined by synchrotron diffraction; (c) and (d) the incorrect combinations of the three measurable <110> edges and the corresponding reciprocals of Equation (3) with surface normal vectors throughout the SST. (For interpretation of the references to colour in this figure legend, the reader is referred to the web version of this article.)

yielded a sufficiently small value of Equation (3). The misorientation between the optimized crystallographic orientation and the microdiffraction measurement is 3.5° with a condition number of 4.0, demonstrating the adequate reliability of the fitting. When the surface normal is close to <111> and is near the upper left side of the SST, all three <110> edges within the {111} planes are observable (see the red point in Fig. 3 as an example). With the three measurable <110> edges, the orientation can be obtained from the SEM images taken at both tilting angles.

When the surface normal is near the right side of the SST (between <111> and <101>), the fraction of the {100} plane in the triple-plane structure is marginal. As a result, only two <110> edges can be measured. Fortunately, by utilizing two tilting angles, the orientation of the grain can still be deduced. Fig. 9 shows the fitting method for a case where there are only two measurable <110> edges. The misorientation between the fitting result and the microdiffraction measurement is only 2.9°, while the condition number of the Jacobian matrix is 13.6, indicating a sound fit.

When the surface normal is along the right boundary in the SST, between <111> and <101>, there is only one measurable <110> edge in this regime, which is inadequate for the deduction of crystallographic orientation (see Fig. 10) However, the orientation of this type of grains can still be determined to be a <1x1> ($0 \leq x \leq 1$) type orientation.

The orientation estimation situations are summarized in Fig. 11. For the majority of the surface normal orientation cases, the projected directions of two or more <110> edges can be precisely measured from SEM images taken at two different tilting angles. Therefore, the Euler angles of these grains can be deduced based on the knowledge of the orientation-dependent surface faceting features discussed previously. Using this method, the misorientation between the fitted crystallographic orientation and the real crystallographic orientation is usually smaller than 5°. However, when the surface normal is along the right boundary of the SST, the orientation cannot be determined, as only one <110> edge is measurable. This validates the assumption made for surface morphology investigation. Additionally, the surface morphology of UO_2 also provides an alternative method of measuring crystallographic orientation of surface grains with acceptable uncertainty only using SE images. In addition to the standard mechanical polishing procedures for SEM/EBSD investigations, this alternative method only requires extra thermal etching at an appropriate temperature for an adequate period (1 h at 1500 °C for UO_2) in an inert gas atmosphere. This is especially meaningful for a nuclear fuel material, the characterization of which is usually restricted due to their radioactivity.

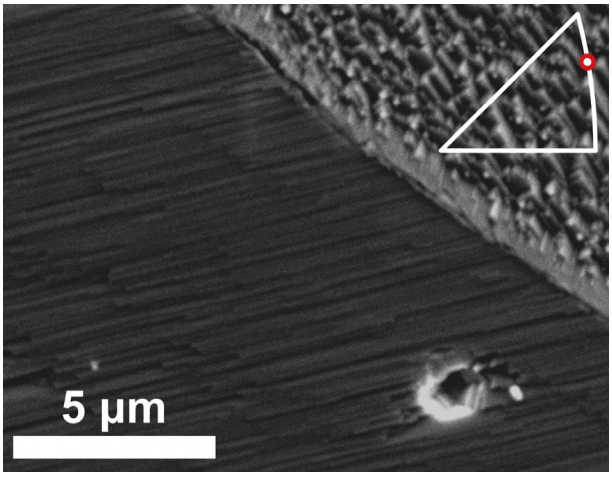

Fig. 10. An SEM image of a typical case near <1x1> surface normal orientation, where there is only one measurable <110> edge. The position of the surface normal in the SST is shown in the upper right corner.

Aside from UO_2, this technique might potentially be applied to other materials. Two prerequisites are required for successful adoption of this method: prominent anisotropy in surface energy and a highly symmetrical crystal structure. The former prerequisite ensures the preferential appearance of some characteristic surface orientations, whereas the latter one helps reduce the complexity in geometry. Thus, this method is expected to work for any cubic materials with large surface energy dependence on crystallographic orientation. On the other hand, for those materials with low-symmetry crystal structures, the determination of crystallographic orientation solely based on surface morphology could be challenging, as the number of different orientations increases greatly in the absence of symmetry reduction.

4. Conclusions

In this study, synchrotron Laue microdiffraction and SEM techniques were collaboratively utilized so as to establish a general correlation between the crystallographic orientation and surface faceting features of polycrystalline UO_2. Sets of low-Miller-index

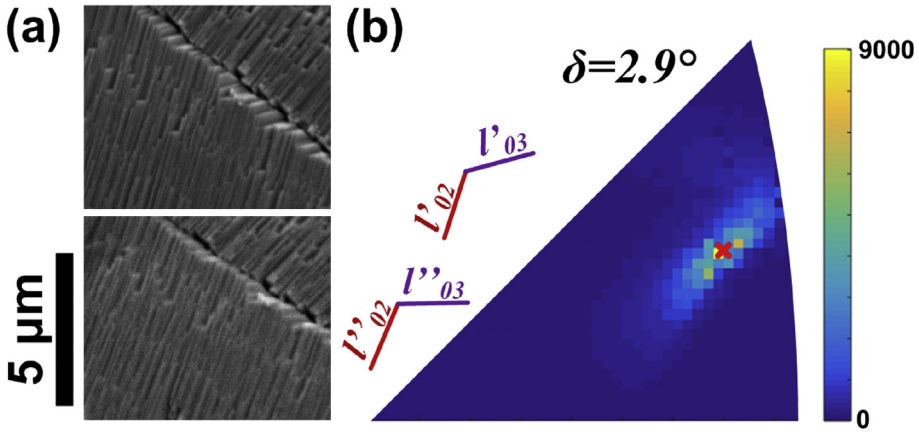

Fig. 9. Fitting details of a typical three-plane feature with two measurable <110> edges: (a) the SEM image of a grain with two measurable <110> edges; (b)the cartoon indicating the two measurable <110> edges in (a) and corresponding reciprocals of Equation (3) with surface normal vectors throughout the SST. The red cross marks the crystallographic orientation determined by synchrotron diffraction. (For interpretation of the references to colour in this figure legend, the reader is referred to the web version of this article.)

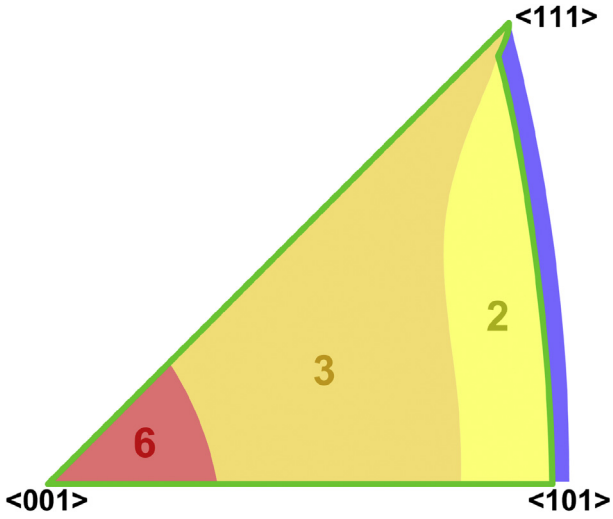

Fig. 11. An SST map summarizing the possibility of determining a grain's crystallographic orientation from SEM images, the regimes outlined in green have sufficient information available from SEM images for orientation determination. The number within each regime indicates the number of measurable <110> edges at a specific tilting angle. The region in blue does not have enough information from SEM images to determine the crystallographic orientation. (For interpretation of the references to colour in this figure legend, the reader is referred to the web version of this article.)

planes were found across the sample, with a dependence upon the surface normal. A triple-plane structure, which contains one {100} plane, two {111} planes, and three <110> edges, is the major surface faceting feature for most orientations. The dominance of this structure can be explained by the preference in thermodynamic preference for low-energy surfaces. The coexistence of {100} and {111} planes on {100} surface also implies the variance of $\gamma_{100}/\gamma_{111}$, probably due to the local fluctuation of surface hydroxidation. The knowledge of the orientation-dependent surface faceting features was used to develop a method to determine the orientation of a grain based on SEM images. This technique is applicable for the vast majority of crystallographic orientations.

Acknowledgments

This work was funded by the U.S. Department of Energy (DOE)'s Nuclear Energy Advanced Modeling and Simulation (NEAMS) program and the U.S. DOE's Nuclear Energy University Program (NEUP) DE-NE0008440. This research used resources of the Advanced Photon Source, a U.S. DOE Office of Science User Facility operated for the DOE Office of Science by Argonne National Laboratory under Contract No. DE-AC-02-06CH11357 between UChicago Argonne, LLC and the U.S. Department of Energy.

References

[1] M. Lyons, R. Boyle, J. Davies, V. Hazel, T. Rowland, UO_2 properties affecting performance, Nucl. Eng. Des. 21 (1972) 167–199.
[2] M. Notley, I.J. Hastings, A microstructure-dependent model for fission product gas release and swelling in UO_2 fuel, Nucl. Eng. Des. 56 (1980) 163–175.
[3] M. Tucker, Grain boundary porosity and gas release in irradiated UO_2, Radiat. Eff. 53 (1980) 251–255.
[4] T. Kutty, K. Chandrasekharan, J. Panakkal, J. Ghosh, Fracture toughness and fracture surface energy of sintered uranium dioxide fuel pellets, J. Mater. Sci. Lett. 6 (1987) 260–262.
[5] K. Forsberg, A. Massih, Diffusion theory of fission gas migration in irradiated nuclear fuel UO_2, J. Nucl. Mater. 135 (1985) 140–148.
[6] J.W. Cahn, C.A. Handwerker, Equilibrium geometries of anisotropic surfaces and interfaces, Mater. Sci. Eng. A 162 (1993) 83–95.
[7] W. Mullins, Theory of linear facet growth during thermal etching, Philos. Mag. 6 (1961) 1313–1341.
[8] E.D. Williams, N.C. Bartelt, Surface faceting and the equilibrium crystal shape, Ultramicroscopy 31 (1989) 36–48.
[9] E.D. Williams, N. Bartelt, Thermodynamics of surface morphology, Science 251 (1991) 393–400.
[10] J.R. Heffelfinger, C.B. Carter, Mechanisms of surface faceting and coarsening, Surf. Sci. 389 (1997) 188–200.
[11] W. Ellis, R. Schwoebel, Leed from surface steps on UO_2 single crystals, Surf. Sci. 11 (1968) 82–98.
[12] W.P. Ellis, Leed studies of UO_2 (111) vicinal surfaces, Surf. Sci. 45 (1974) 569–584.
[13] T. Taylor, W. Ellis, A leed study of UO_2 (100) vicinal surfaces, Surf. Sci. 77 (1978) 321–336.
[14] V. Kraševec, B. Navinšek, Faceting of UO_2 single crystal surfaces, Physica Status Solidi (a) 30 (1975) 501–509.
[15] M. Abramowski, R.W. Grimes, S. Owens, Morphology of UO_2, J. Nucl. Mater. 275 (1999) 12–18.
[16] F.N. Skomurski, R.C. Ewing, A.L. Rohl, J.D. Gale, U. Becker, Quantum mechanical vs. empirical potential modeling of uranium dioxide (UO_2) surfaces: (111),(110), and (100), Am. Mineralogist 91 (2006) 1761–1772.
[17] S. Dudarev, M. Castell, G. Botton, S. Savrasov, C. Muggelberg, G. Briggs, A. Sutton, D. Goddard, Understanding STM images and eels spectra of oxides with strongly correlated electrons: a comparison of nickel and uranium oxides, Micron 31 (2000) 363–372.
[18] W. Van Lierde, On the surface free energy anisotropy of UO_2, J. Mater. Sci. 5 (1970) 527–531.
[19] M.R. Castell, Wulff shape of microscopic voids in UO_2 crystals, Phys. Rev. B 68 (2003) 235411.
[20] A.H. Tan, M. Abramowski, R.W. Grimes, S. Owens, Surface defect configurations on the (100) dipolar surface of UO_2, Phys. Rev. B 72 (2005) 035457.
[21] A.H. Tan, R.W. Grimes, S. Owens, Structures of UO_2 and PuO_2 surfaces with hydroxide coverage, J. Nucl. Mater. 344 (2005) 13–16.
[22] M. Castell, C. Muggelberg, G. Briggs, D. Goddard, Scanning tunneling microscopy of the UO_2(111) surface, J. Vac. Sci. Technol. B 14 (1996) 966–969.
[23] C. Muggelberg, M. Castell, G. Briggs, D. Goddard, An STM study of the UO_2(001) surface, Appl. Surf. Sci. 142 (1999) 124–128.
[24] K. Mo, Z. Zhou, Y. Miao, D. Yun, H.-M. Tung, G. Zhang, W. Chen, J. Almer, J.F. Stubbins, Synchrotron study on load partitioning between ferrite/martensite and nanoparticles of a 9cr ods steel, J. Nucl. Mater 455 (2014) 376–381.
[25] Y. Miao, K. Mo, Z. Zhou, X. Liu, K.-C. Lan, G. Zhang, M.K. Miller, K.A. Powers, J. Almer, J.F. Stubbins, In situ synchrotron tensile investigations on the phase responses within an oxide dispersion-strengthened (ods) 304 steel, Mater. Sci. Eng. A 625 (2015) 146–152.
[26] Y. Miao, K. Mo, Z. Zhou, X. Liu, K.-C. Lan, G. Zhang, M.K. Miller, K.A. Powers, Z.-G. Mei, J.-S. Park, et al., On the microstructure and strengthening mechanism in oxide dispersion-strengthened 316 steel: a coordinated electron microscopy, atom probe tomography and in-situ synchrotron tensile investigation, Mater. Sci. Eng. A 639 (2015) 585–596.
[27] Y. Miao, K. Mo, B. Cui, W.-Y. Chen, M.K. Miller, K.A. Powers, V. McCreary, D. Gross, J. Almer, I.M. Robertson, et al., The interfacial orientation relationship of oxide nanoparticles in a hafnium-containing oxide dispersion-strengthened austenitic stainless steel, Mater. Charact. 101 (2015) 136–143.
[28] G. Zhang, Z. Zhou, K. Mo, Y. Miao, X. Liu, J. Almer, J.F. Stubbins, The evolution of internal stress and dislocation during tensile deformation in a 9cr ferritic/martensitic (f/m) ods steel investigated by high-energy x-rays, J. Nucl. Mater. 467 (2015) 50–57.
[29] G. Zhang, K. Mo, Y. Miao, X. Liu, J. Almer, Z. Zhou, J.F. Stubbins, Load partitioning between ferrite/martensite and dispersed nanoparticles of a 9cr ferritic/martensitic (f/m) ods steel at high temperatures, Mater. Sci. Eng. A 637 (2015) 75–81.
[30] D. Brown, D. Alexander, K. Clarke, B. Clausen, M. Okuniewski, T. Sisneros, Elastic properties of rolled uranium–10wt.% molybdenum nuclear fuel foils, Scr. Mater 69 (2013) 666–669.
[31] Y. Miao, K. Mo, B. Ye, L. Jamison, Z.-G. Mei, J. Gan, B. Miller, J. Madden, J.-S. Park, J. Almer, et al., High-energy synchrotron study of in-pile-irradiated u–mo fuels, Scr. Mater. 114 (2016) 146–150.
[32] D. Yun, Y. Miao, R. Xu, Z. Mei, K. Mo, W. Mohamed, B. Ye, M.J. Pellin, A.M. Yacout, Characterization of high energy xe ion irradiation effects in single crystal molybdenum with depth-resolved synchrotron microbeam diffraction, J. Nucl. Mater. 471 (2016) 272–279.
[33] J.-S. Chung, G.E. Ice, Automated indexing for texture and strain measurement with broad-bandpass x-ray microbeams, J. Appl. Phys. 86 (1999) 5249–5255.
[34] T. Yao, S.M. Scott, G. Xin, J. Lian, Tio_2 doped UO_2 fuels sintered by spark plasma sintering, J. Nucl. Mater. 469 (2016) 251–261.
[35] K. Teske, H. Ullmann, D. Rettig, Investigation of the oxygen activity of oxide fuels and fuel-fission product systems by solid electrolyte techniques. part I: Qualification and limitations of the method, J. Nucl. Mater. 116 (1983) 260–266.
[36] T. Wangle, V. Tyrpekl, M. Cologna, J. Somers, Simulated UO_2 fuel containing csi by spark plasma sintering, J. Nucl. Mater. 466 (2015) 150–153.